JOURNAL OF SPACECRAFT AND ROCKETS
Vol. 34, No. 1, January–February 1997

Computational Fluid Dynamics Simulation of Turbulent Waverider Flowfield with Sideslip

Yijian Shi* and John B. Miles†
University of Missouri–Columbia, Columbia, Missouri 65211
and
Kakkattukuzhy Isaac‡
University of Missouri–Rolla, Rolla, Missouri 65409-1350

To better understand the waverider hypersonic flowfield with sideslip, the flowfield computational fluid dynamics simulation for a selected waverider at 5-deg angle of sideslip off-design condition is conducted. The off-design flowfield is more complicated than the nominal design, inasmuch as there is very strong shock-wave/boundary-layer interaction at the windward waverider tip, and a detached shock at the leeward tip, whether the flow conditions are inviscid or viscous. For these different simulations, the pressure coefficient distribution basically has the same values except near the tip, but the shock attachment point on the lower surface and force coefficient value are different. The shock-wave/boundary-layer interaction and shock attachment pattern at the windward tip strongly affect the waverider pressure and local skin-friction coefficient distribution in that region. The simulated pressure coefficient distribution is in good agreement with available experimental results.

Nomenclature

A_b	= base area, m^2
C_D	= forebody drag coefficient (with $P_b = p_\infty$), $D/(\frac{1}{2}\rho_\infty U_\infty^2)$
C_f	= local skin-friction coefficient, $\tau/(\frac{1}{2}\rho_\infty U_\infty^2)$
C_L	= forebody lift coefficient, $L/(\frac{1}{2}\rho_\infty U_\infty^2)$
C_p	= pressure coefficient, $(p - p_\infty)/(\frac{1}{2}\rho_\infty U_\infty^2)$
F, G, H	= inviscid flux terms
H_v	= viscous flux term
M	= Mach number
P_b	= base pressure, Pa
Pr	= Prandtl number
p	= pressure, Pa
$\boldsymbol{Q}$	= conserved variable vector in generalized coordinates
Re	= Reynolds number
T	= temperature, K
t	= time, s
U_∞	= freestream velocity, m/s
u, v, w	= velocity components in x_i, m/s
x^i	= generalized coordinates, $[\psi, \eta, \zeta]^t$
x_i	= Cartesian coordinates, $[x, y, z]^t$
α	= angle of attack, deg
β	= angle of sideslip, deg
μ	= total viscosity $(\mu_l + \mu_t)$, kg/m·s
μ_l	= laminar viscosity, kg/m·s
μ_t	= turbulent viscosity, kg/m·s
ρ	= density, kg/m^3
τ	= shear stress, $\mu\{[\mathrm{d}\sqrt{(u^2 + v^2 + w^2)}]/\mathrm{d}n\}$, Pa
$()_\infty$	= freestream

Introduction

WAVERIDER design and flowfield analyses have become more advanced in recent years. In the early 1980s, a series of waverider forebody configurations[1,2] with curved surfaces was derived from known inviscid conical flows. Later on, viscous optimized hypersonic waverider configurations[3] were obtained. All these configurations have some remarkable features such as higher lift-to-drag ratio in hypersonic flight, because they are designed to efficiently use the high pressure on their lower surfaces resulting from strong oblique shocks. Engine–airframe integration[4] and inlet design[5] for these configurations have recently been presented.

This paper will focus on a particular waverider flowfield analysis, rather than on various different waverider design shapes. The Euler (inviscid),[6] laminar,[7] and turbulent[8] waverider flowfields for the selected shape under the nominal design conditions, at which shock waves are supposed to be exactly attached at waverider tips, were simulated earlier. Off-design waverider flowfield analyses[9,10] considering viscous effects, and variation of angle of attack and Mach number have also been conducted. Stability derivatives for hypersonic waveriders calculated according to Newtonian theory have recently been reported in Ref. 11. The flowfield features with angle of sideslip will be analyzed, which is very important because flight at nonzero angle of sideslip is inevitable and more complicated, e.g., takeoff and landing in cross wind, turning, and unsymmetrical thrust flight. The resultant flowfield for this case is no longer symmetrical about the waverider geometrical plane of symmetry. Therefore, a grid for the entire waverider forebody, rather than for half of it as previously considered,[7–9] is needed. The resulting larger grid size will require more computer CPU time and memory.

To better understand waverider flowfields, a relatively simple Rasmussen waverider forebody configuration[2] is chosen. The lower surface of this configuration (Fig. 1) can be expressed by a closed mathematical formula, and the upper surfaces are intersecting planes. This waverider configuration satisfies the more demanding

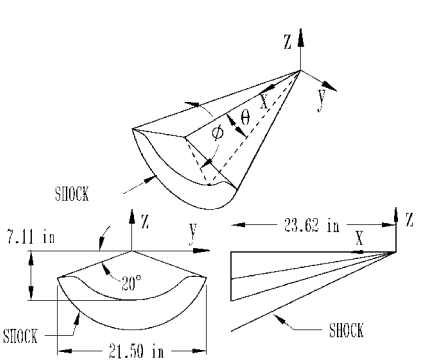

Fig. 1 Geometry of the conical waverider.

Received Nov. 21, 1995; revision received Aug. 25, 1996; accepted for publication Aug. 28, 1996. Copyright © 1996 by the American Institute of Aeronautics and Astronautics, Inc. All rights reserved.

*Graduate Student, Mechanical and Aerospace Engineering.
†Professor, Mechanical and Aerospace Engineering. Senior Member AIAA.
‡Associate Professor, Mechanical and Aerospace Engineering. Associate Fellow AIAA.

internal volume requirement of waveriders. In addition, some useful experimental results for this configuration have already been obtained[12,13] and are available for comparison purposes. For the selected waverider configuration shown in Fig. 1, the nominal design conditions are as follows: freestream Mach number $M_\infty = 4$, angle of attack $\alpha = 0$ deg, and angle of sideslip $\beta = 0$ deg. If the flight meets the nominal design conditions, an oblique shock wave should be created and exactly attached at the waverider leading edges. However, if the flight does not satisfy the nominal design conditions (off-design conditions), the created shock could be either attached to the waverider surfaces or detached from them, as discussed in Ref. 9.

Using Roe's flux-difference splitting numerical scheme,[14] the Baldwin–Lomax algebraic turbulence model,[15] and time-averaged thin-layer Navier–Stokes equation,[16] as embodied in the CFL3D code, the off-design waverider flowfield simulation with $M_\infty = 4$, $\alpha = 0$ deg, and $\beta = 5$ deg, including Euler, laminar, and turbulent cases, has been conducted and will be discussed. Force coefficients, local skin-friction and pressure coefficient distributions, and pressure and Mach number contours will be presented. Other conditions chosen are as follows: freestream Reynolds number $Re = 5.08 \times 10^6$/ft, freestream temperature $T_\infty = 520$ R, Prandtl number $Pr = 0.72$, adiabatic wall, and the ideal-gas assumption. These conditions are consistent with the conditions in Ref. 8 and partially consistent with the conditions in Refs. 7, 12, and 13. In Ref. 7, the Reynolds number, $Re = 2 \times 10^6$/ft was used, which could better fit the laminar-flow simulation and is in the range of experimental values given in Refs. 12 and 13. For the simulation to best meet the turbulent flow conditions, the Reynolds number selected for this study is increased to the value of 5.08×10^6/ft. For air, the Prandtl number, $Pr = 0.72$, and the ideal-gas assumption generally are reasonable choices for the Mach numbers considered. Moreover, to focus on off-design flow analyses and simplify the extent of computational parameters, the adiabatic wall is assumed, which is widely used in supersonic aerodynamic analyses. This assumption becomes restrictive only when considering aerodynamic heating, which is outside the scope of the present study.

Governing Equations and Turbulence Model

The thin-layer time-averaged Navier–Stokes governing equations[16] to be satisfied are given by Eq. (1), written in generalized coordinates and conservative form. The generalized coordinates in the equation are with respect to the Cartesian variable

$$\frac{\partial}{\partial t}(\boldsymbol{Q}) + \frac{\partial}{\partial \xi}(\boldsymbol{F}) + \frac{\partial}{\partial \eta}(\boldsymbol{G}) + \frac{\partial}{\partial \zeta}(\boldsymbol{H} - \boldsymbol{H}_v) = 0 \qquad (1)$$

The total viscosity μ implicitly contained in Eq. (1) is defined as $\mu = \mu_l + \mu_t$, and the laminar viscosity (or molecular viscosity) is described by Sutherland's law as a function of temperature. The eddy viscosity μ_t is modeled using the Baldwin–Lomax algebraic turbulence model.[15]

Numerical Algorithm and Grid Generation

To solve Eq. (1), the approximate Riemann solver of Roe[14] is used for the numerical representation of the inviscid fluxes. The quantity $\boldsymbol{Q}$ in the inviscid fluxes is obtained by using MUSCL for interpolation of the primitive variables ρ, u, v, w, and p. Second-order central differencing is used for viscous fluxes.

Because the flowfields to be analyzed are not symmetrical, a three-dimensional grid has to be generated for the entire waverider forebody. As a result of grid sensitivity studies conducted to eliminate solution sensitivity to grid size, the size of the three-dimensional grid is chosen as $51 \times 146 \times 71$ in the streamwise, circumferential, and normal directions, respectively, with a very fine mesh distribution in the vicinity of the leading edge and the nose. The two-dimensional grid at the waverider baseplane, as shown in Fig. 2, is generated by using a differential equation method.[17] The entire three-dimensional grid is then obtained by extending the two-dimensional grid to the nose of the waverider, using linear interpolation techniques.[18] To guarantee sufficiently precise skin-friction predictions and minimize solution sensitivity to grid size in this grid generation process,

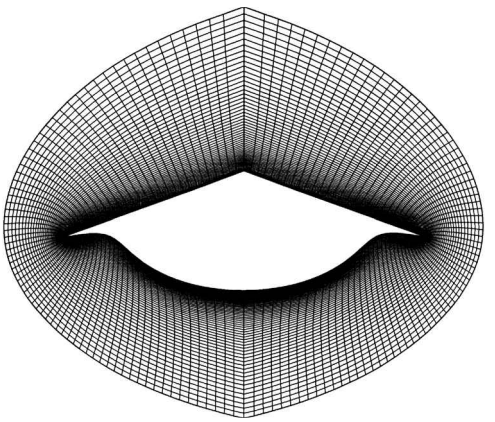

Fig. 2 Two-dimensional grid at the waverider baseplane.

there must be an adequate number of grid points in the laminar sublayer of the turbulent boundary layer. Accordingly, about five grid points are located in the laminar sublayer.[18] The no-slip and impermeable wall conditions were imposed in the present calculations. The outer-boundary conditions were specified as the freestream flow property. The initial flow conditions were specified as those of the uniform freestream flow.

Results and Discussion

The off-design waverider flowfields with the conditions $\alpha = 0$, $\beta = 5$ deg, $M_\infty = 4$, $Re = 5.08 \times 10^6$/ft, $T_\infty = 520$ R, and adiabatic wall, for Euler, laminar, and turbulent cases, are simulated and discussed. The present simulation results are compared with experimental data and other computational fluid dynamics (CFD) simulation results.

Euler Solution

The Euler solutions for the $\beta = 5$ deg waverider are shown in Figs. 3–10. The pressure ratio p/p_∞, defined as the ratio of the local pressure to the freestream pressure, is shown in Fig. 3. The shock on the lower surface can be clearly seen. The shock is detached from the leeward waverider tip and attached to the lower surface near the windward tip. The attachment pattern of the shock at the windward tip, which is more clearly seen in the blow-up view in Fig. 4, is very similar to that shown in Refs. 6 and 9 for the $M_\infty = 5$ off-design case. These results also appear in Fig. 13.6 in a recent textbook by Rasmussen.[19]

In Fig. 4, besides the main shock attached to the lower surface, there is a weak oblique shock attached at the tip, which is obviously generated by the tip outboard of the main shock. In addition, on the waverider upper surface, differences in the flowfields on either side of the centerline can be observed from Fig. 3. The flow is slightly compressed on the windward upper surface and expanded on the leeward upper surface. These results are caused by the angles formed between the approaching flow and the upper surface, as shown in Fig. 5. The windward upper surface functions like a wedge with the angle Φ, which satisfies $\Phi = \sin^{-1}(\sin 20 \sin \beta) = 1.7$ deg for $\beta = 5$ deg used in the present case; i.e., the freestream undergoes a 1.7-deg compression. Because the angle Φ is so small, the compression shown in Fig. 3 is very weak. Similarly, the expansion on the leeward upper surface, resulting from the flow around a corner of a very small deflection angle, is also very weak.

The pressure coefficient distribution is shown in Fig. 6. For comparison purposes, the on-design results are also plotted. Obviously, the off-design and on-design results are greatly different. The off-design waverider has higher pressure coefficient on the windward lower and upper surfaces, and lower pressure coefficient on the leeward lower and upper surfaces. There are two pressure jumps at the windward tip region for the off-design waverider, caused by the strong shock and the weak shock as analyzed earlier, respectively. From $y = 3$ to 0 in., the pressure on the upper surface slightly decreases. This decrease results from the effects of the lower pressure on the leeward upper surface, because that region is enclosed in the Mach cone of the upper stream disturbances.

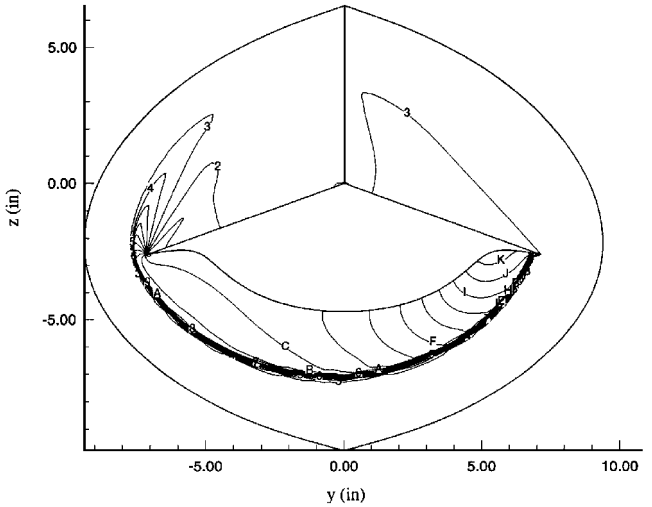

Fig. 3 Pressure ratio (p/p_∞) contours for the Euler waverider at x = 15.67 in. Level press: K, 4.7056; J, 4.4902; I, 4.2748; H, 4.0594; G, 3.844; F, 3.6286; E, 3.4132; D, 3.1978; C, 2.9824; B, 2.767; A, 2.5516; 9, 2.3362; 8, 2.1208; 7, 1.9054; 6, 1.69; 5, 1.4746; 4, 1.2592; 3, 1.0438; 2, 0.8284; and 1, 0.613.

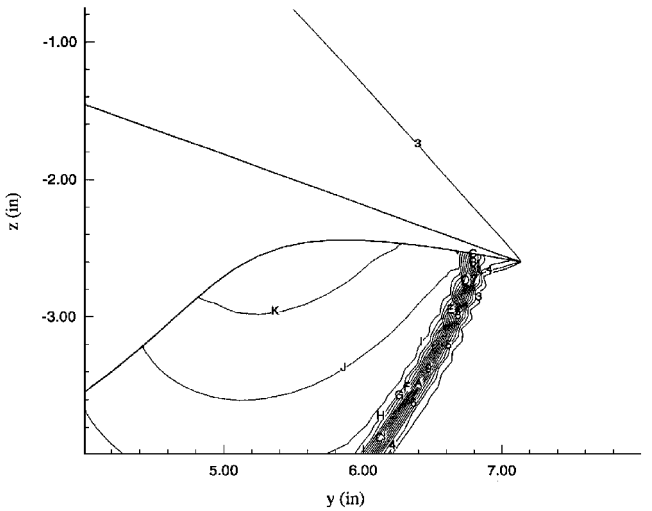

Fig. 4 Blow-up of pressure ratio (p/p_∞) contours near the windward tip for the Euler waverider at x = 15.67 in. Level press: K, 4.7056; J, 4.4902; I, 4.2748; H, 4.0594; G, 3.844; F, 3.6286; E, 3.4132; D, 3.1978; C, 2.9824; B, 2.767; A, 2.5516; 9, 2.3362; 8, 2.1208; 7, 1.9054; 6, 1.69; 5, 1.4746; 4, 1.2592; 3, 1.0438; 2, 0.8284; and 1, 0.613.

Figure 7 shows the Mach number contours. The Mach number is slightly decreased on the windward upper surface and increased on the leeward upper surface. From the windward tip to the leeward tip on the lower surface, the Mach number gradually goes up.

Figure 8 shows the temperature ratio (T/T_∞) contours. The temperature ratio (T/T_∞) is slightly increased on the windward upper surface and decreased above the leeward upper surface. From the windward tip to the leeward tip on the lower surface, the temperature ratio (T/T_∞) basically goes down. These variations are all explainable by the pressure effects discussed earlier. However, not all of the observed phenomena are simple and easily explainable. For example, a detailed analysis of the flow on the leeward upper surface near the tip region would be very challenging. The pressure coefficient variation in that region shown in Fig. 6 is irregular. To better understand this behavior, the simplified general flow on the upper surface is plotted in Fig. 9. The flow is divided into four regions, A, B, C, and D. In region A, the freestream gets a slight compression, then some of the compressed flow, as represented by the line a, obtains a slight expansion in region B when passing around the centerline. In region D, the freestream is strongly compressed after passing through the detached shock, then the flow traverses the expansion waves at the leeward tip, which results from both the

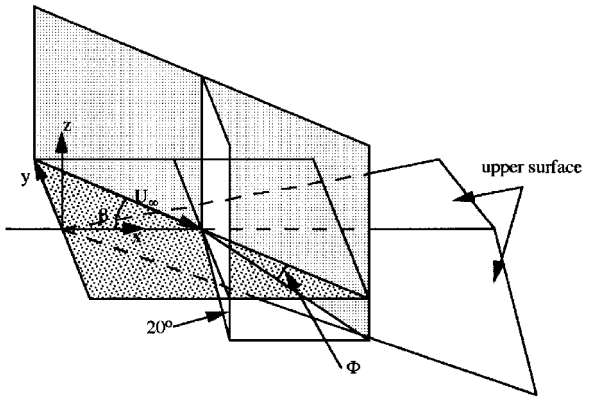

Fig. 5 Angles formed between the upper surface and freestream.

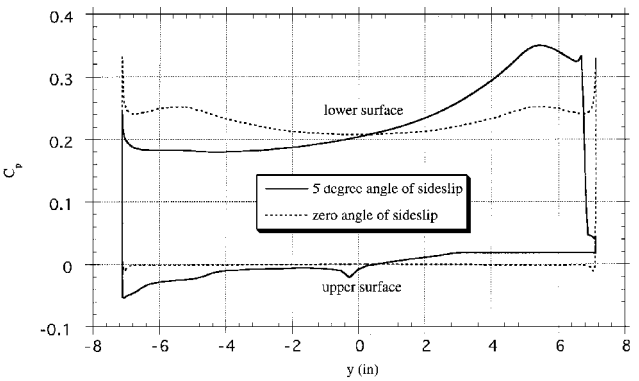

Fig. 6 Circumferential variation of the pressure coefficient for the Euler waverider at x = 15.67 in.

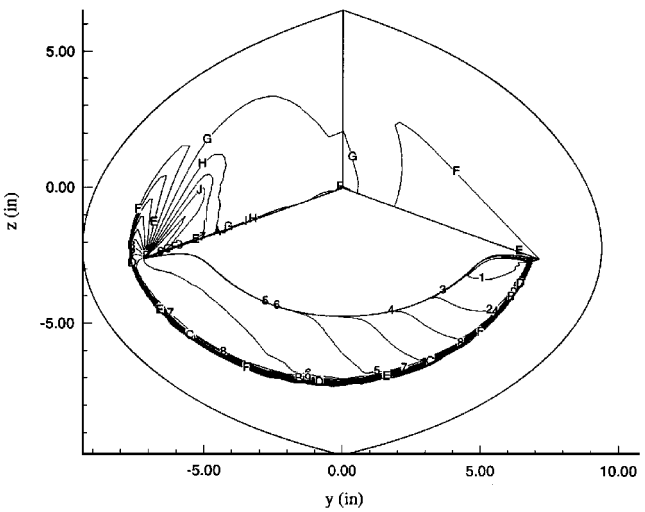

Fig. 7 Mach number contours for the Euler waverider at x = 15.67 in. Level Mach: K, 4.34343; J, 4.25886; I, 4.17429; H, 4.08971; G, 4.00514; F, 3.92057; E, 3.836; D, 3.75143; C, 3.66686; B, 3.58229; A, 3.49771; 9, 3.41314; 8, 3.32857; 7, 3.244; 6, 3.15943; 5, 3.07486; 4, 2.99029; 3, 2.90571; 2, 2.82114; and 1, 2.73657.

shock and the geometry of the upper surface, and enters region C, as represented by the line b. So far, we can firmly conclude that the flow in different regions has different features, which could include the velocity direction, velocity magnitude, Mach number, temperature, or pressure. Therefore, the flow on the leeward upper surface is very complicated. This complication will cause irregular changes of the local skin-friction coefficient for the laminar waverider (shown later). Because of the flow interactions among different regions and three-dimensional effects (for example, the shock is not uniform in strength and not planar), some flow phenomena may be beyond explanation.

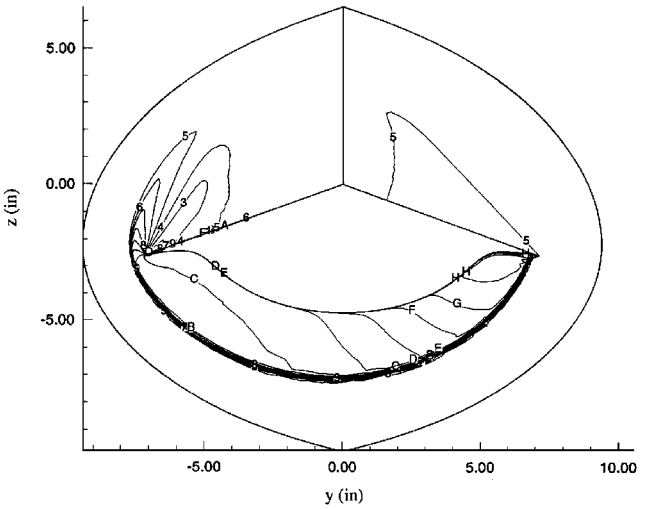

Fig. 8 Temperature ratio (T/T_∞) contours for the Euler waverider at x = 15.67 in. Level T: K, 1.83222; J, 1.77845; I, 1.72467; H, 1.6709; G, 1.61712; F, 1.56334; E, 1.50957; D, 1.45579; C, 1.40201; B, 1.34824; A, 1.29446; 9, 1.24069; 8, 1.18691; 7, 1.13313; 6, 1.07936; 5, 1.02558; 4, 0.971805; 3, 0.918029; 2, 0.864252; and 1, 0.810476.

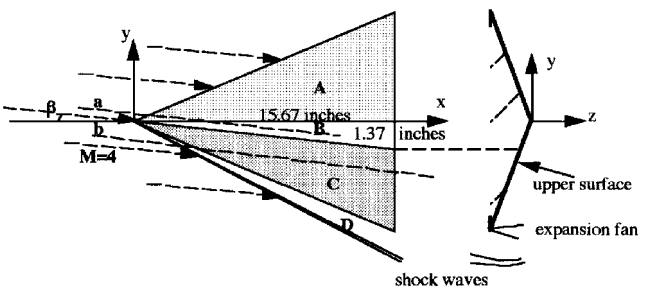

Fig. 9 Flow on the waverider upper surface.

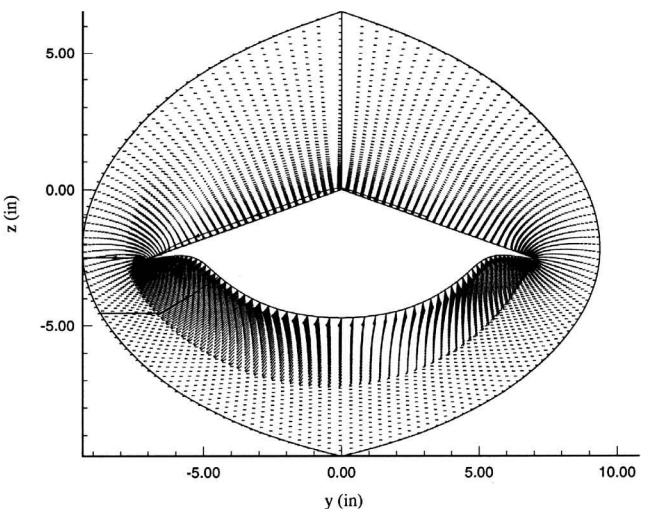

Fig. 10 Cross-plane velocity vectors for the Euler waverider at x = 15.67 in.

The crossflow velocity vectors are shown in Fig. 10. Obviously, the flow is not symmetrical. The flow velocity vectors in the centerline vicinity on the lower surface are significantly misaligned from the x direction, and although there is a detached shock at the leeward tip, there is no longer a separation bubble near the leeward tip on the upper surface, as discussed in Ref. 9.

Laminar Solution

The laminar waverider solutions are presented in Figs. 11–14. Figure 11 shows the pressure ratio p/p_∞ contours. The shock on the lower surface is as well captured as in the Euler solution. The

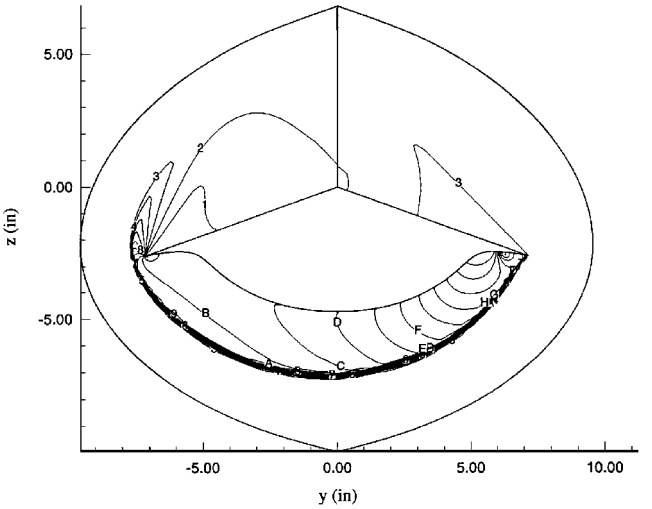

Fig. 11 Pressure ratio (p/p_∞) contours for the laminar waverider at x = 15.67 in. Level press: K, 4.75755; J, 4.5481; I, 4.33864; H, 4.12919; G, 3.91974; F, 3.71029; E, 3.50083; D, 3.29138; C, 3.08193; B, 2.87248; A, 2.66302; 9, 2.45357; 8, 2.24412; 7, 2.03467; 6, 1.82521; 5, 1.61576; 4, 1.40631; 3, 1.19686; 2, 0.987405; and 1, 0.777952.

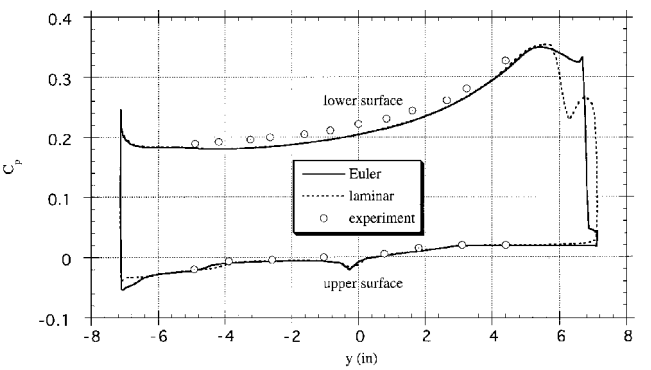

Fig. 12 Circumferential variation of the pressure coefficient: lines, CFD at x = 15.67 in.; symbols, at x = 15.57 in., $Re = 2 \times 10^6$/ft, M_∞ = 4, α = 0 deg, and β = 5 deg.

shock is detached at the leeward waverider tip, as with the Euler solution. However, it is attached at the windward waverider tip, which is different from the Euler solution. The shock attachment pattern at the windward tip is very similar to the attachment pattern shown in Ref. 9 for the $M_\infty = 5$ off-design case. Therefore, from the analyses in Ref. 9, the attachment pattern, including the pressure gradients on the windward lower surface, is caused by the laminar boundary-layer/shock-wave interaction. On the waverider upper and lower surfaces, the pressure trends shown in Fig. 11 are similar to the Euler results. The flow is slightly compressed on the windward upper surface and expanded on the leeward upper surface. The flow on the lower surface is gradually expanded from windward to leeward.

The circumferential variation of pressure coefficient is shown in Fig. 12. For comparison purposes, the Euler solution and experimental results[13] are also plotted. The pressure variation near the lower windward tip region in Fig. 12 surprisingly matches what was shown in Ref. 9 for the $M_\infty = 5$ off-design case. This pressure variation is a typical pattern of the laminar boundary-layer/shock-wave interaction in that region. In addition, the pressure distribution on the leeward upper surface is slightly different from the Euler result. In comparison with the experimental results, good agreement can be seen. Unfortunately, experimental results near the tip regions, which would be valuable for comparison, are not available.

Figure 13 shows the Mach number contours. By comparing to the Euler solution, there is no significant difference except near the surface. Because of viscosity, the flow near the surface becomes more complicated and has lower Mach number.

Figure 14 shows comparison of the variation of local skin-friction coefficient between the off-design and on-design laminar

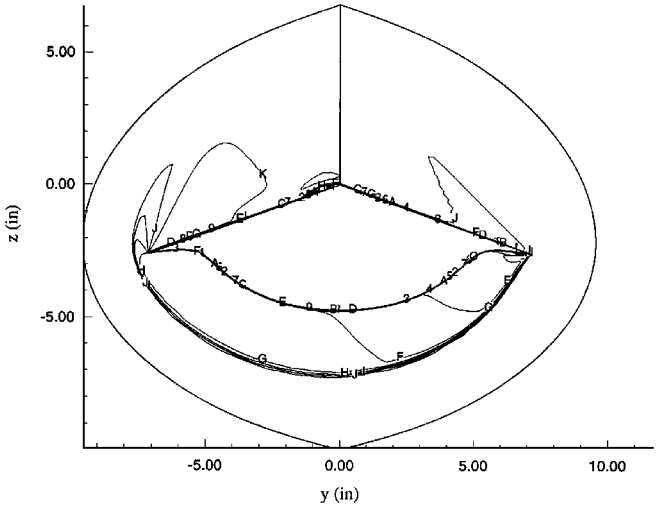

Fig. 13 Mach number contours for the laminar waverider at x = 15.67 in. Level Mach: K, 4.05048; J, 3.84795; I, 3.64543; H, 3.4429; G, 3.24038; F, 3.03786; E, 2.83533; D, 2.63281; C, 2.43029; B, 2.22776; A, 2.02524; 9, 1.82271; 8, 1.62019; 7, 1.41767; 6, 1.21514; 5, 1.01262; 4, 0.810095; 3, 0.607571; 2, 0.405048; and 1, 0.202524.

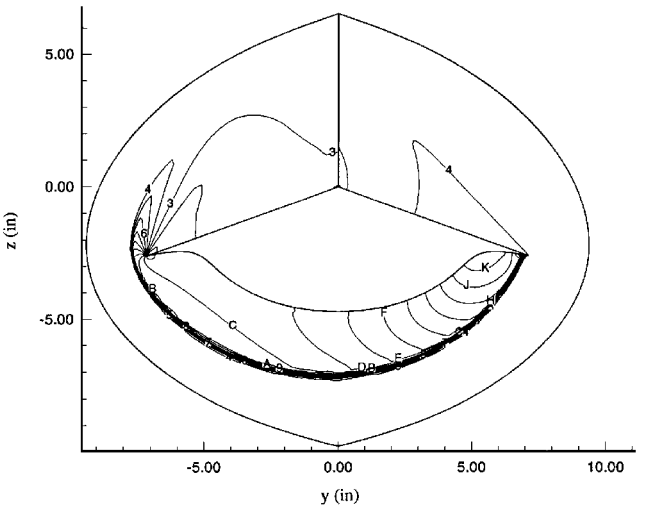

Fig. 15 Pressure ratio (p/p) contours for the turbulent waverider at x = 15.67 in. Level press: K, 4.66766; J, 4.45147; I, 4.23527; H, 4.01908; G, 3.80289; F, 3.5867; E, 3.3705; D, 3.15431; C, 2.93812; B, 2.72193; A, 2.50573; 9, 2.28954; 8, 2.07335; 7, 1.85716; 6, 1.64096; 5, 1.42477; 4, 1.20858; 3, 0.992385; 2, 0.776193; and 1, 0.56.

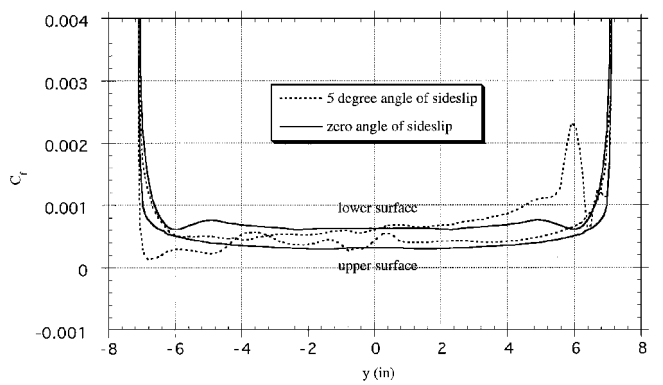

Fig. 14 Circumferential variation of the local skin friction coefficient for the laminar waverider at x = 15.67 in.

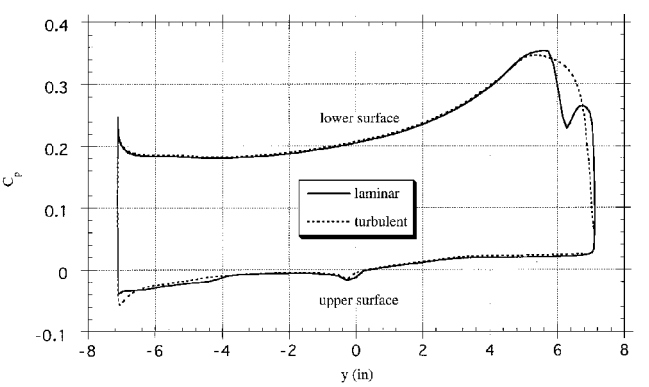

Fig. 16 Circumferential variation of the pressure coefficient at x = 15.67 in.

waveriders. Because of the Mach number changes, the values of the local skin-friction coefficient for the off-design waverider are higher on the windward surfaces and lower on the leeward lower surface than for the on-design waverider. In the windward tip region on the lower surface, the changes in the skin friction are very similar to that shown and well discussed in Ref. 9 for the $M_\infty = 5$ off-design case. On the leeward upper surface, the trends in the skin-friction variation are very complicated. It is difficult to explain this phenomenon, because the flow in that region is complicated and the skin friction is very sensitive to flow features, further complicated by the three-dimensional effects and the interaction of different flows.

Turbulent Solution

The turbulent waverider solutions are shown in Figs. 15–18. Figure 15 shows the pressure ratio p/p_∞ contours. The shock on the lower surface is well captured. The shock is detached at the leeward waverider tip, but attached at the windward tip, which is different from the Euler and laminar solutions given in Figs. 3 and 11, respectively. In comparison with Fig. 11, there are complicated pressure gradients for the turbulent waverider near the tip on the windward lower surface in Fig. 15. The strong attached shock at the tip in Fig. 15 indicates that the propagation of the pressure disturbance, as discussed in Ref. 9 for the $M_\infty = 5$ off-design case, strengthens this shock. Additionally, because of stronger energy exchanges in the turbulent boundary layer than in the laminar boundary layer, which tends to smooth the pressure variation, the propagation of the pressure disturbance results in smoother pressure distribution in the tip vicinity on the windward lower surface. On the waverider surfaces, the pressure trends shown in Fig. 15 are similar to the Euler and laminar results. The flow is slightly compressed on the windward upper surface and expanded on the leeward upper surface. The flow on the lower surface is gradually expanded from windward to leeward.

The shock-wave/boundary-layer interaction discussed can comprehensively be reflected in the pressure coefficient distribution around the windward waverider tip, as shown in Fig. 16. From Fig. 16, the pressure coefficient of the turbulent waverider near the tip region on the windward lower surface is quite different from those of the laminar and Euler waveriders. There is no pressure jump on the windward lower surface for the turbulent waverider as observed for the Euler waverider in Fig. 6, because of the shock-wave/boundary-layer interaction. However, there is a simple pressure gradient near the tip on the lower surface for the turbulent waverider because of stronger energy exchanges in the turbulent boundary layer, rather than the complicated ones seen for the laminar waverider. The other difference among the Euler, laminar, and turbulent solutions is on the leeward upper surface wherein the turbulent solution has lower pressure coefficient values at the tip. This difference verifies that turbulent flow has a stronger capability to overcome an adverse pressure gradient than a laminar flow, because the turbulent pressure coefficient is in better agreement with the Euler solution at that location, as shown in Fig. 6. Except for these tip regions, the pressure coefficient of the turbulent waverider is in good agreement with that of the laminar waverider.

Figure 17 shows the Mach number contours. By comparing to the Euler and laminar solutions, we see that they are basically similar, except near the surface. First of all, because the turbulent boundary layer is thicker than the laminar boundary layer, the turbulent waverider has a dark thick region formed by overlapped contour lines near the surfaces than the laminar waverider, as observed by comparing Fig. 17 to Fig. 13. In the centerline vicinity on the upper

Table 1 Force coefficients

Condition	C_D	C_L	C_L/C_D
Euler	0	0.763	3.468
Laminar	0.226	0.762	3.372
Turbulent	0.241	0.763	3.166

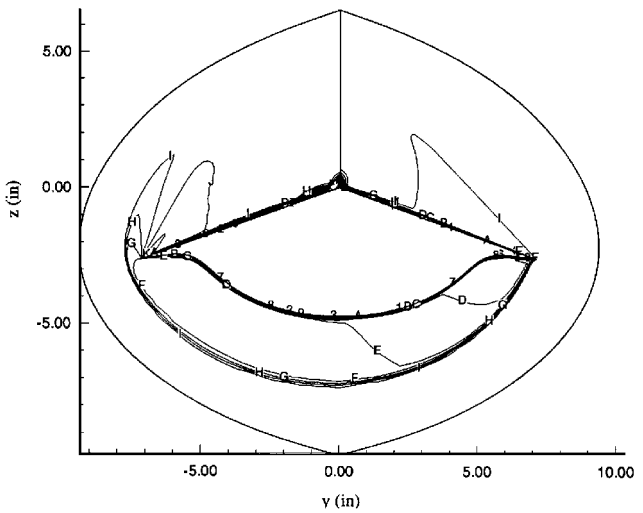

Fig. 17 Mach number contours for the turbulent waverider at x = 15.67 in. Level Mach: K, 4.3; J, 4.08474; I, 3.86947; H, 3.65421; G, 3.43895; F, 3.22368; E, 3.00842; D, 2.79316; C, 2.57789; B, 2.36263; A, 2.14737; 9, 1.93211; 8, 1.71684; 7, 1.50158; 6, 1.28632; 5, 1.07105; 4, 0.85579; 3, 0.640526; 2, 0.425263; and 1, 0.21.

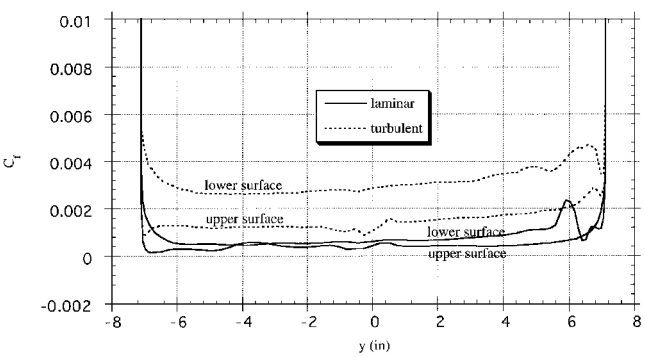

Fig. 18 Circumferential variation of the local skin friction coefficient at x = 15.67 in.

surface, the flow has very interesting gradients. These gradients could be caused by the interference of the local and upstream turbulent boundary layers between the region B and A near the centerline shown in Fig. 9, in which there are very strong energy exchanges across the centerline.

Figure 18 shows the comparison of the local skin-friction coefficients between the turbulent and laminar waveriders. The trends of the local skin-friction coefficients are different near the tip region on the windward lower surface. However, the trends for the turbulent waverider in that region are consistent with the pressure trends as shown in Fig. 16. Surprisingly, the changes of the local skin-friction coefficients on the leeward upper surface for the turbulent waverider are simpler than for the laminar waverider. The eddy viscosity smears the skin-friction fluctuations because of strong energy exchanges in the boundary layer.

Body-Force Coefficient

The force coefficients are presented in Table 1. For different flow patterns, the lift coefficient C_L has slight variations but the drag coefficient C_D has considerable changes. For the off-design waverider, the Euler case has the highest C_L/C_D value because of the lowest C_D and the turbulent case has the lowest C_L/C_D value because of the highest C_D. Unfortunately, experimental results are not available for comparison. However, compared to the nominal design results,[8] the values of C_L, C_D, and C_L/C_D have only slight changes.

Conclusions

The flowfield for the $\beta = 5$ deg waverider is more complicated in comparison with other cases. However, most of the phenomena can be well explained. The flow on the leeward upper surface is too complex to give detailed explanations, especially for the laminar waverider. At the leeward tip of the $\beta = 5$ deg waverider, the shocks are completely detached on the lower surfaces, whether the flow type is Euler, laminar, or turbulent. However, at the windward tip of the waverider, the shocks are clearly attached. However, for the different flow types, the shock attachment pattern on the lower surfaces is quite different. The main shock for the Euler case is attached at the lower surface, rather than at the tip, although there is another very weak shock attached at the tip. Because of the shock-wave/boundary-layer interaction, the attached shocks for the laminar and turbulent waveriders are generated at the tip. Thus, for the off-design waveriders, the shock-wave/boundary-layer interaction is a significant phenomenon. It affects not only the attachment pattern of the shocks, but also the pressure coefficient distribution and local skin-friction coefficient. Moreover, the effects of the shock-wave/boundary-layer interaction on the shock attachment pattern, the pressure coefficient distribution, and the local skin-friction coefficient are different for the laminar and turbulent flow cases. Because of strong energy exchanges in the turbulent boundary layer, the resultant shock-wave/boundary-layer interaction is simpler than in the laminar case. The simulated values of the pressure coefficient are in good agreement with available experimental results. Generally speaking, the pressure coefficient is not sensitive to the flow conditions used in the present simulation. The Euler, laminar, and turbulent waveriders basically have the same values of the pressure coefficient, except in the tip vicinity. However, the local skin-friction coefficient is very sensitive to the viscous flow conditions. For different flow conditions, C_L has slight variation, but C_D has considerable changes. The Euler case has the highest C_L/C_D value because of the lowest C_D, and the turbulent case has the lowest C_L/C_D value because of the highest C_D. Compared to the nominal design results, the values of C_L, C_D, and C_L/C_D have only slight changes.

The analyses presented are very important toward further understanding waverider flowfields. The waverider is still in the developing stage. Various new waverider forebody configurations are being derived. Therefore, the present results would be useful for understanding waverider flowfields and considering scramjet design, aerodynamic heating, separated flow, vehicle handling and control, vehicle stability, and afterbody design.

Acknowledgments

We thank the University of Missouri Research Board for providing financial support for this work. We also thank the National Center for Supercomputer Applications, University of Illinois, for a Cray YMP grant for conducting the present computational fluid dynamics simulation, and James Thomas, NASA Langley Research Center, for providing the CFL3D code. The grid system has been generated by extending the grid generation procedure used in GRAPE, a computer program written at the NASA Ames Research Center.

References

[1] Jischke, M. C., "Supersonic Flow Past Conical Bodies with Nearly Circular Cross Sections," *AIAA Journal*, Vol. 19, No. 2, 1981, pp. 242–245.

[2] Rasmussen, M. L., "Waverider Configurations Derived from Inclined Circular and Elliptic Cones," *Journal of Spacecraft and Rockets*, Vol. 17, No. 6, 1980, pp. 537–545.

[3] Bowcutt, K. G., Anderson, J. D., and Capriotti, D., "Viscous Optimized Hypersonic Waveriders," AIAA Paper 87-0272, Jan. 1987.

[4] Hemdan, H. T., and Jischke, M. C., "Inlets for Waveriders Derived from Elliptic-Cone Stream Surfaces," *Journal of Spacecraft and Rockets*, Vol. 24, No. 1, 1987, pp. 23–32.

[5] O'Neill, M. K. L., and Lewis, M. J., "Optimized Scramjet Integration on a Waverider," *Journal of Aircraft*, Vol. 29, No. 6, 1992, pp. 1114–1121.

[6] Yoon, B. H., and Rasmussen, M. L., "Computational Analysis of Hypersonic Flows Past Elliptic-Cone Waveriders," Univ. of Oklahoma, Research Rept. OU-AME-91-2, Norman, OK, Jan. 1991.

[7]Liao, J. R., Isaac, K. M., Miles, J. B., and Tsai, B. J., "Navier–Stokes Simulation for Cone-Derived Waverider," *AIAA Journal*, Vol. 30, No. 6, 1992, pp. 1521–1528.

[8]Tsai, B. J., Miles, J. B., and Isaac, K. M., "Computation of Turbulent Flow About Cone-Derived Waverider," AIAA Paper 92-2726, Dec. 1992.

[9]Shi, Y., Tsai, B. J., Miles, J. B., and Isaac, K. M., "Cone-Derived Waverider Flowfield Simulation Including Turbulence and Off-Design Conditions," *Journal of Spacecraft and Rockets*, Vol. 33, No. 2, 1996, pp. 185–190.

[10]Takashima, N., and Lewis, M. J., "Navier–Stokes Computation of a Viscous-Optimized Waverider," *Journal of Spacecraft and Rockets*, Vol. 31, No. 3, 1994, pp. 383–391.

[11]Rasmussen, M. L., "Stability Derivatives for Hypersonic Waveriders According to Newtonian Theory," AIAA Paper 95-3492, Aug. 1995.

[12]Rasmussen, M. L., Jischke, M. C., and Daniel, D. C., "Experimental Forces and Moments on Cone-Derived Waveriders for $M_\infty = 3$ to 5," *Journal of Spacecraft and Rockets*, Vol. 19, No. 6, 1982, pp. 592–598.

[13]Jischke, M. C., Rasmussen, M. L., and Daniel, D. C., "Experimental Surface Pressures on Cone-Derived Waveriders for $M_\infty = 3$–5," *Journal of Spacecraft and Rockets*, Vol. 20, No. 6, 1983, pp. 539–545.

[14]Roe, P. L., "Approximate Riemann Solvers, Parameter Vectors and Difference Schemes," *Journal of Computational Physics*, Vol. 43, No. 2, 1981, pp. 357–372.

[15]Baldwin, B. S., and Lomax, H., "Thin-Layer Approximation and Algebraic Model for Separated Turbulent Flows," AIAA Paper 78-257, Jan. 1978.

[16]Anderson, D. A., Tannehill, J. C., and Pletcher, R. H., *Computational Fluid Mechanics and Heat Transfer*, 1st ed., Hemisphere, New York, 1984, pp. 190–197, 421–424.

[17]Sorenson, R. L., "A Computer Program to Generate Two-Dimensional Grids About Airfoils and Other Shapes by the Use of Poisson's Equation," NASA TM 81198, May 1980.

[18]Shi, Y., "Off-Design Waverider Flowfield CFD Simulation," Ph.D. Dissertation, Dept. of Mechanical and Aerospace Engineering, Univ. of Missouri, Columbia, MO, May 1996.

[19]Rasmussen, M. L., *Hypersonic Flow*, Wiley-Interscience, New York, 1994, Chap. 13.

K. J. Weilmuenster
Associate Editor